

## Electron acceleration by turbulent plasmoid reconnection

X. Zhou,<sup>1, a)</sup> J. Büchner,<sup>1</sup> F. Widmer,<sup>1, b)</sup> and P. A. Muñoz<sup>1</sup>

*Max Planck Institute for Solar System Research, Justus-von-Liebig-Weg 3,  
37077 Göttingen, Germany*

(Dated: 4 April 2022)

In space and astrophysical plasmas, like in planetary magnetospheres, as that of Mercury, energetic electrons are often found near current sheets (CSs), which hints at electron acceleration by magnetic reconnection. Unfortunately, electron acceleration by reconnection is not well understood, yet. In particular, acceleration by turbulent plasmoid reconnection. We have investigated electron acceleration by turbulent plasmoid reconnection, described by MHD simulations, via test particle calculations. In order to avoid resolving all relevant turbulence scales down to the dissipation scales, a mean-field turbulence model is used to describe the turbulence of sub-grid scales (SGS) and their effects via a turbulent electromotive force (EMF). The mean-field model describes the turbulent EMF as a function of the mean values of current density, vorticity, magnetic field as well as of the energy, cross-helicity and residual helicity of the turbulence. We found that, mainly around X-points of turbulent reconnection, strongly enhanced localized EMFs most efficiently accelerated electrons and caused the formation of power-law spectra. Magnetic-field-aligned EMFs, caused by the turbulence, dominate the electron acceleration process. Scaling the acceleration processes to parameters of the Hermean magnetotail, electron energies up to 60 keV can be reached by turbulent plasmoid reconnection through the thermal plasma.

---

<sup>a)</sup>zhou@mps.mpg.de; Also at Key Laboratory of Dark Matter and Space Astronomy, Purple Mountain Observatory, Chinese Academy of Sciences, Nanjing, 210008, China.

<sup>b)</sup>Presently at CEA, IRFM, F-13108 Saint Paul-Lez-Durance, France

## I. INTRODUCTION

Energetic electrons are observed remotely and in-situ throughout the whole solar system and beyond. They are accelerated during solar flares as well as in planetary magnetospheres and so on. Since high-energy electrons are often found near current sheets (CSs), magnetic reconnection is thought to be one key process for their acceleration. On the other hand, collisionless space plasmas are usually highly turbulent. The consequences of turbulence and magnetic reconnection for electron acceleration, however, are not well understood, yet.

Different models have been proposed to take into account turbulence in magnetic reconnection, e.g., Refs. 1 and 2 and test particle studies have been carried out to investigate the particle acceleration resulting from MHD-turbulent magnetic reconnection. *Ambrosiano et al.*<sup>3</sup> found efficient particle energization by two dimensional (2D) turbulent magnetic reconnection. *Dmitruk et al.*<sup>4</sup> carried out test particle studies in 3D turbulent magnetic reconnection, which revealed a preferential electron acceleration parallel to the magnetic field in localized current sheets. *Petkaki & MacKinnon*<sup>5,6</sup>, *Burge et al.*<sup>7</sup> analysed the consequences of turbulent electromagnetic fields on particle acceleration at X-type neutral points. They found an increasing energization in strong turbulence and formation of bi-modal (double-peak) distributions. *Kowal et al.*<sup>8</sup> studied proton acceleration in 3D turbulent CSs. They found that the proton acceleration rate was highly enhanced by a first-order Fermi process due to contracting magnetic fluctuations. These prior calculations, however, did not consider the effects of turbulence in sub-grid-scales due to the limitation of the computing resources. *Yoshizawa*<sup>9</sup> proposed a mean-field turbulence model to describe the effects of small-scale turbulence on the large-scale dynamics. Recently, *Yokoi & Hoshino*<sup>10</sup> suggested their consequences to turbulent magnetic reconnection via an electromotive force (EMF). The EMFs in this mean-field turbulence model are related to the mean current density, vorticity, magnetic field as well as to the energy, cross-helicity and residual helicity of the MHD turbulence. In the present work, we use this mean-turbulence model to investigate electron acceleration by turbulent plasmoid reconnection with parameters of the Hermean magnetotail. Energetic electrons have been observed in-situ in the turbulent plasma of the Hermean magnetotail, their acceleration mechanisms are, however, less understood compared to the energetic electrons in the Earth's magnetotail<sup>11</sup>.

Mercury is the closest planet to the Sun with a quite weak and small magnetosphere.

On the other hand, it has the most dynamical magnetosphere among all the four terrestrial planets. Several spacecrafts have been devoted to investigate the environment of Mercury: Mariner 10, the two Helios spacecrafts, the MErcury Surface, Space ENvironment, GEochemistry and Ranging (MESSENGER) mission with its Energetic Particle Spectrometer (EPS), the X-Ray Spectrometer (XRS), the Gamma-Ray and Neutron Spectrometer (GRNS) as well as the Gamma Ray Spectrometer (GRS). The first in-situ measurements of the energetic particles at Mercury were made by Mariner 10 in 1974-75. Mariner 10 discovered that energetic electron bursts in the Hermean magnetotail have a time duration of about  $10\text{ s}$ <sup>12</sup>. Pileup in the instrument electronics of the Mariner 10, however, led overestimations of the particle energies<sup>13</sup>. Later, the MESSENGER (starting 2011) regularly observed energetic electrons with energies up to 100-200 keV in the Hermean magnetotail, while the typical particle energy in the upstream solar wind are typically only 1.5 - 10 keV based on the observation of the Helios spacecraft<sup>14</sup>. Observations of the MESSENGER provide a strong evidence for electron acceleration in the Hermean magnetotail. The MESSENGER, however, did not find energetic ions<sup>15-18</sup>. Various acceleration mechanisms have been proposed to explain these observed high electron energies in the Hermean magnetotail: inductive acceleration via substorm-like dipolarization<sup>19</sup>, stochastic acceleration, wave-particle interactions, bow-shock energization, and magnetic reconnection in the magnetotail (see *Zelenyi et al.*<sup>20,21</sup>). MESSENGER discovered not only clear signatures of energetic electrons but also multiple plasmoids and plasmoid reconnection in the Hermean magnetotail<sup>22-24</sup>. We followed these observations using characteristic parameters of the Hermean magnetotail, plasmoid reconnection and plasma turbulence, since plasmas with high Reynolds number, typical for astrophysical environments, are prone to be turbulent<sup>1</sup>.

Theoretical analyses<sup>25,26</sup>, observations<sup>27,28</sup>, MHD and particle-in-cell (PIC)-code simulations<sup>29,30</sup> have shown that fast magnetic reconnection can be due to plasmoid instabilities forming magnetic islands (or flux ropes) in elongated current sheets with finite guide field in the direction perpendicular to the reconnection plane. To describe the influence of turbulence in sub-grid-scales on plasmoid reconnection, *Widmer et al.*<sup>31</sup> recently used the mean-field turbulence model of *Yoshizawa*<sup>9</sup> and *Yokoi & Hoshino*<sup>10</sup>. They found that turbulence can enhance reconnection rates in dependence on the properties of the turbulence.

Electron acceleration by plasmoid reconnection has been investigated previously via theoretical analyses<sup>32,33</sup> and PIC code simulations<sup>32,34,35</sup>. Those studies revealed the importance

of the curvature and gradient drifts by contraction and coalescence of plasmoids. Test particle calculations<sup>36–38</sup> partially confirmed this prediction, however, without considering the consequences of turbulence. In this study, we investigate the consequences of EMF caused by turbulence on electron acceleration in plasmoid-unstable CSs by using the mean-field turbulence model of *Yoshizawa*<sup>9</sup> and *Yokoi & Hoshino*<sup>10</sup>. The relevant mean electromagnetic fields are obtained by a Gaussian spatial filtering<sup>31,39</sup>. We carried out test particle calculations in the macroscopic (mean) fields based on a relativistic guiding center approximation.

This paper is organized as follows. In Section II, we describe the high resolution MHD simulations of plasmoid-unstable CSs and the mean-field turbulence model of *Yoshizawa*<sup>9</sup> and *Yokoi & Hoshino*<sup>10</sup>. In Section III, we reveal the resulting electron acceleration in plasmoid-unstable CSs, discriminate the different physical effects on electron energization and localize the electron acceleration sites. Characteristic trajectories of the strongest energized electrons as well as the resulting electron energy spectra are provided in Section III. Conclusions and discussions are contained in Section IV.

## II. PLASMOID RECONNECTION AND TURBULENCE

### A. Plasmoid reconnection

In this section we present the MHD simulations that we used for our electron acceleration calculations (see also of *Widmer et al.*<sup>31</sup>). Our MHD simulations describe the evolution of the electromagnetic fields of plasmoid-unstable CSs by solving the following set of resistive MHD equations:

$$\frac{\partial \rho}{\partial t} = -\nabla \cdot (\rho \vec{U}) \quad (1)$$

$$\frac{\partial \rho \vec{U}}{\partial t} = -\nabla \cdot [\rho \vec{U} \vec{U} + \frac{1}{2}(p + \frac{B^2}{\mu_0})\mathbf{I} - \frac{\vec{B}\vec{B}}{\mu_0}] + \chi \nabla^2 \rho \vec{U} \quad (2)$$

$$\frac{\partial \vec{B}}{\partial t} = \nabla \times (\vec{U} \times \vec{B} - \eta \vec{J}) \quad (3)$$

$$\frac{\partial h}{\partial t} = -\nabla \cdot (h \vec{U}) + \frac{\gamma_0 - 1}{2\gamma_0 h^{\gamma_0 - 1}} \eta J^2 + \chi \nabla^2 h, \quad (4)$$

using the GOEMHD3 code<sup>31,40</sup>. Here  $\rho$  is the mass density,  $\vec{U}$  is the plasma velocity,  $\mathbf{I}$  is the three-dimensional identity matrix,  $\vec{B}$  is the magnetic field and  $h$  is related to the thermal pressure  $p$  via  $p = 2h^{\gamma_0}$ , with  $\gamma_0 = 5/3$  being the ratio of specific heats in adiabatic

conditions. Ampère's law is used to compute the current density  $\vec{J} = \nabla \times \vec{B}/\mu_0$ , with  $\mu_0$  being the vacuum magnetic permeability. A small homogeneous (normalized) resistivity  $\eta = 0.001$  corresponds to a sufficiently large magnetic Reynolds number, so that a plasmoid instability takes place<sup>41</sup> (see below for the normalization of the resistivity).  $\chi$  in Eqs. (2) and (4) represents the amount of local viscosity switched on as soon as any numerical instability starts. The variables in Eqs. (1) to (4) are dimensionless. In order to be applied to the typical Mercury conditions, The variables in Eqs. (1) to (4) are normalized to values characteristic for the Hermean magnetotail<sup>20,21,42</sup>, in the MHD simulation: the length scale is the assumed halfwidth of the Hermean magnetotail CS  $L_0 = 2.5 \times 10^4 m$ , the magnetic field is  $B_0 = 7.5 \times 10^{-8} T$ , and the typical Alfvén transit time is  $t_0 = 1 s$ . All other normalizations can be derived from the above three normalizing quantities: velocities are normalized to  $V_0 = L_0/t_0 = 2.5 \times 10^4 m/s$ , electric fields to  $E_0 = V_0 B_0 = 1.9 \times 10^{-3} V/m$ , the current densities to  $J_0 = B_0/(\mu_0 L_0) = 2.4 \times 10^{-6} A/m^2$  and the resistivity to  $\eta_0 = \mu_0 L_0 V_0 = 7.9 \times 10^2 \Omega \cdot m$ .

In these simulations, an almost two-dimensional simulation box containing  $4 \times 3200 \times 12800$  grid points in a domain  $L_X \times L_Y \times L_Z = 0.4 \times 80 \times 320 L_0^3$ , where  $X, Y$  and  $Z$  are the directions out of the CS plane, across and along the CS, respectively. The MHD simulation uses periodic boundary conditions in the  $Y$  and  $Z$  directions. Double Harris-type CSs with a finite guide field  $b_g = B_{x0}/B_0$  are initialized as follows (in dimensionless units):

$$\vec{B} = b_g \vec{e}_x + [\tanh(y+d) - \tanh(y-d) - 1] \vec{e}_z \quad (5)$$

$$h = \frac{1}{2} (1 + \beta_p - B^2)^{1/\gamma_0} \quad (6)$$

Here we will further present results obtained for a guide magnetic field  $b_g = 2$ .  $\beta_p = 0.5$  is the plasma- $\beta$  (ratio between thermal and magnetic pressures), the half-distance between the two CSs is  $d = 20$  and the symbols  $\vec{e}_j$  denote the unit vectors in the directions  $j = x, y$  or  $z$ . A multi-mode initial perturbation spectrum is used to trigger the plasmoid instability:

$$B_y(z) = \sum_{k=1}^{128} 0.01 \lambda_1 \sin \left[ 2\pi k \left( \frac{z}{L_z} + \lambda_2 \right) \right] \quad (7)$$

where  $\lambda_1$  and  $\lambda_2$  are random numbers in the range  $[0, 1]$ <sup>31</sup>.

## B. Mean-field approach of turbulence

In a mean-field approach<sup>39,43</sup>, the induction equation (Eq. 3) becomes

$$\partial_t \vec{B} = -\nabla \times \vec{E} = \nabla \times \left( \vec{U} \times \vec{B} - \eta \vec{J} - \vec{\varepsilon}_M \right) \quad (8)$$

where  $\vec{\varepsilon}_M$  denotes the EMF, due to the turbulence. We apply the turbulence model, proposed by *Yoshizawa*<sup>9</sup> and *Yokoi & Hoshino*<sup>10</sup> to obtain  $\vec{\varepsilon}_M$ . In that model, the EMF  $\vec{\varepsilon}_M$  is obtained as a function of the mean current density  $\vec{J}$ , the vorticity  $\vec{\Omega}$  ( $\vec{\Omega} = \nabla \times \vec{U}$ ) and the mean magnetic field  $\vec{B}$ :

$$\vec{\varepsilon}_M = \mu_0 \beta \vec{J} - \omega \sqrt{\mu_0 \rho} \vec{\Omega} - \alpha \vec{B} \quad (9)$$

In the model of *Yoshizawa*<sup>9</sup> and *Yokoi & Hoshino*<sup>10</sup>, the  $\beta$  term in the EMF plays the role of a turbulent diffusion while the  $\alpha$  term corresponds to the usual dynamo term that accounts for a possible magnetic field generation or at least its sustainment against diffusion. It appears due to the inhomogeneous flow effects on turbulence. Coupled with the vorticity  $\vec{\Omega}$ , the  $\omega$  term accounts for the contribution of the the vorticity to the EMF. Depending on its relative signature compared to the  $\beta$  term, this term might act as an additional dynamo term<sup>44</sup>. A complete description of Eq. (9) as well as the physical meaning of the coefficients  $\beta, \omega$  and  $\alpha$  can be found in Ref. 45. According to *Yoshizawa*<sup>9</sup> and *Yokoi & Hoshino*<sup>10</sup>, the coefficients  $\beta, \omega$  and  $\alpha$  in Eq. (9) are related to the (normalized) turbulent energy density  $K$ , cross-helicity density  $W$  and residual helicity  $H$  as

$$\beta = \tau C_\beta K, \quad \omega = \tau C_\omega W, \quad \alpha = \tau C_\alpha H \quad (10)$$

where  $C_\beta, C_\omega$  and  $C_\alpha$  are constants of the order of  $10^{-2} - 10^{-1}$ <sup>9,46-48</sup> and  $\tau$  is the characteristic decay time of the turbulence. In a lowest order approximation,  $\tau$  can be considered to be constant and of the order of the initial Alfvén transit time ( $\tau = 1$  or  $2 t_0$ ), i.e., the time needed for an Alfvén wave to cross the initial CS. This is a simplified approach for  $\tau$  based on previous studies of magnetic reconnection which revealed the highest reconnection rates. In their configurations, the fastest magnetic reconnection due to mean-field turbulence effects was found for  $\tau \sim 1.0 - 2.0$  (e.g., Refs. 41 and 48). Turbulent energy  $K$ , cross-helicity  $W$

and residual helicity  $H$  are defined as

$$\begin{aligned}
K &= \frac{1}{2} \left[ \left( \overline{U^2} - \overline{U}^2 \right) + \frac{\overline{B^2} - \overline{B}^2}{\mu_0 \bar{\rho}} \right] \\
W &= \frac{\overline{\vec{U} \cdot \vec{B}} - \overline{\vec{U}} \cdot \overline{\vec{B}}}{\sqrt{\mu_0 \bar{\rho}}} \\
H &= - \left( \overline{\vec{U} \cdot \vec{\Omega}} - \overline{\vec{U}} \cdot \overline{\vec{\Omega}} \right) + \frac{\overline{\vec{B} \cdot \vec{J}} - \overline{\vec{B}} \cdot \overline{\vec{J}}}{\bar{\rho}}
\end{aligned} \tag{11}$$

Combining Eqs. (8) to (9), the mean electric field  $\overline{\vec{E}}$  reads

$$\begin{aligned}
\overline{\vec{E}} &= -\overline{\vec{U}} \times \overline{\vec{B}} + \eta \overline{\vec{J}} + \overrightarrow{\varepsilon_M} \\
&= -\overline{\vec{U}} \times \overline{\vec{B}} + (\eta + \mu_0 \beta) \overline{\vec{J}} - \omega \sqrt{\mu_0 \bar{\rho}} \overline{\vec{\Omega}} - \alpha \overline{\vec{B}}
\end{aligned} \tag{12}$$

In this mean-field approach, for plasmas with high magnetic Reynolds numbers (small  $\eta$ ), annihilation of the magnetic fluxes is solely due to the turbulence by the  $\beta$ -related term, which allows the collisionless plasmas to have a possibility to undergo magnetic reconnection. In addition, the  $\omega$ - and  $\alpha$ -terms lead to (dynamo-)generation (or sustainment) of magnetic fields<sup>10</sup>.

We use a filter function  $\Gamma(\vec{r}, \vec{r}')$  to obtain the mean component  $\overline{F}$  of a quantity  $F$ :

$$\overline{F(\vec{r})} = \int \Gamma(\vec{r}, \vec{r}') F(\vec{r}') d\vec{r}' \tag{13}$$

For the filtering, we choose a Gaussian filter with a kernel function<sup>31,39</sup>:

$$\Gamma(\vec{r}, \vec{r}') = \left( \frac{6}{\pi \Delta^2} \right)^{3/2} \exp \left[ -\frac{(\vec{r} - \vec{r}')^2}{\Delta^2/6} \right] \tag{14}$$

where  $\Delta$  is the filter width. For  $\Delta = 4$  (grid size), the Reynolds rules<sup>49</sup> ( $\overline{\overline{F}} = \overline{F}$ ,  $\overline{f'} = 0$  and  $\overline{f' \overline{F}} = 0$ , here  $F = \overline{F} + f'$ ) are satisfied best. From here onwards, the variables used for the electromagnetic fields will be replaced by their mean values and the symbol ' $\overline{\phantom{x}}$ ' for the mean fields will be omitted.

According to the mean-field turbulence theory (see Eq. 12),  $C_\beta > C_\omega$  and  $C_\beta > C_\alpha$  cause diffusion rather than generation of magnetic fields. In this case, the turbulent EMF  $\overrightarrow{\varepsilon_M}$  will accelerate particles. Larger  $C_\beta$  and  $\tau$  correspond to a larger EMF  $\overrightarrow{\varepsilon_M}$ , which causes fast magnetic flux annihilation and reconnection<sup>10,31</sup>. We use  $C_\omega = 0.04$ ,  $C_\alpha = 0.001$  (see *Widmer et al.*<sup>31</sup>) and investigate the influence of the turbulence on electron acceleration by varying  $C_\beta$

| Case      | A | B    | C   | D   | E   |
|-----------|---|------|-----|-----|-----|
| $C_\beta$ | 0 | 0.05 | 0.5 | 0.5 | 1.0 |
| $\tau$    | 0 | 1.0  | 1.0 | 2.0 | 1.0 |

TABLE I. Turbulence parameters used in our calculations.

(=0.05, 0.5, 1.0) and  $\tau$  (=1.0, 2.0), see Table I, due to the  $\beta \propto \tau C_\beta$  term in Eq. (9) plays the role of transporting energies from the magnetic fields to the plasma and particles. We varied the turbulence model parameters because the actual valid theoretical values for  $C_\beta$  and  $\tau$  have not been derived, yet. What is known from the turbulence theory is that  $C_\beta$  should be of the order of  $O(10^{-2} - 10^{-1})$ . For  $\tau$ , it is known that more efficient reconnection is for  $\tau \sim 1.0 - 2.0$ <sup>41,48</sup>. Case A with  $C_\beta, \tau = 0$  is chosen for comparison with the limited case where turbulence is neglected, i.e., laminar reconnection<sup>50</sup> where the magnetic flux annihilation is not affected by turbulence. Note that  $C_\beta$  in Case E is out of the range  $10^{-2} - 10^{-1}$ . This investigation allows to reveal the importance of the  $\omega$ - and  $\alpha$ -terms (Eq. (12)) comparing its outcome with that of Cases D and E. The coefficients  $\tau C_\alpha$  and  $\tau C_\omega$  in Case D are two times as large as those of Case E for the  $\omega$ - and  $\alpha$ -terms, while their coefficient  $\tau C_\beta = 1$  for the  $\beta$ -term are same. Note that the  $\beta$ -term can be balanced by the  $\omega$ - and  $\alpha$ -terms<sup>10,31</sup>. Larger  $\omega$ - and  $\alpha$ -terms for the same  $\beta$ -term correspond to a smaller EMF  $\vec{\varepsilon}_M$  and weaker magnetic flux annihilation. Magnetic flux annihilation, therefore, decreases from Case E to Case A. The maximum reconnection electric field  $[(\eta + \beta)\vec{J} - \omega\vec{\Omega} - \alpha\vec{B}]$  in Case E is about  $1.3 E_0 \sim 2.5 \text{ mV/m}$ .

The results which are presented in the following are obtained for the CS centered at  $y = -d = -20$ . The evolution of the mean magnetic field in this CS is depicted in the top panels of Fig. 1. The first (last) panel depicts the initial (final) CS configuration. The bottom panel of Fig. 1 shows a stack plot for the time evolution of the out-of-plane component of the vector potential  $A_x$  along the CS center. Local minima of  $A_x$  (black and light blue colors) indicate X-points, while the local maxima of  $A_x$  (magenta and red colors) correspond to the centers of plasmoids (O-points).  $A_x$  is a proxy of the electric field. Smaller values of  $A_x$  indicate stronger electric fields. With the help of the stack plots in Fig. 1, one can identify contraction, coalescence and expansion of the plasmoids as well as the formation of secondary plasmoids (indicated by the splitting of black or light-blue regions) in the course



of the nonlinear evolution of the plasmoid instability.

### III. ELECTRON ACCELERATION

#### A. Test particle method

Due to the overall finite guide magnetic field ( $b_g = 2$ ), a (relativistic) guiding center approximation can be used to describe the electron motion. Its applicability can be proven by calculating the adiabaticity parameter  $\kappa = R_{min}/\rho_{max}$ , where  $R_{min}$  and  $\rho_{max}$  are the minimum curvature radius of the magnetic fields and the maximum Larmor radius of each electron<sup>51,52</sup>. Transition from adiabatic motion to chaotic scattering is controlled by  $\kappa$ : for adiabatic electrons,  $\kappa$  should be larger than 3. For smaller  $\kappa$ , the guiding center approximation is not valid<sup>19</sup>. In our study,  $\kappa$  is always larger than 9 for all electrons, i.e., the guiding center approximation is appropriate for this investigation.

The relevant guiding center equations of motion to be solved are<sup>36,53,54</sup>:

$$\frac{d\vec{R}}{dt} = \vec{v}_D + \frac{\gamma v_{\parallel}}{\gamma} \vec{b} \quad (15)$$

$$\begin{aligned} \vec{v}_D = \vec{v}_E &+ \frac{m}{q} \frac{(\gamma v_{\parallel})^2}{\gamma k^2 B} [\vec{b} \times (\vec{b} \cdot \nabla) \vec{b}] + \frac{m}{q} \frac{\mu}{\gamma k^2 B} [\vec{b} \times (\nabla(kB))] \\ &+ \frac{m}{q} \frac{\gamma v_{\parallel}}{k^2 B} [\vec{b} \times (\vec{b} \cdot \nabla) \vec{v}_E] + \frac{m}{q} \frac{\gamma v_{\parallel}}{k^2 B} [\vec{b} \times (\vec{v}_E \cdot \nabla) \vec{b}] \\ &+ \frac{m}{q} \frac{\gamma}{k^2 B} [\vec{b} \times (\vec{v}_E \cdot \nabla) \vec{v}_E] + \frac{1}{\gamma c^2} \frac{E_{\parallel}}{k^2 B} (\gamma v_{\parallel}) (\vec{b} \times \vec{v}_E) \\ &+ \frac{m}{q} \frac{\gamma v_{\parallel}}{k^2 B} (\vec{b} \times \frac{\partial \vec{b}}{\partial t}) + \frac{m}{q} \frac{\gamma}{k^2 B} (\vec{b} \times \frac{\partial \vec{v}_E}{\partial t}) \end{aligned} \quad (16)$$

$$\begin{aligned} \frac{d(\gamma v_{\parallel})}{dt} &= \frac{q}{m} E_{\parallel} - \frac{\mu}{\gamma} [\vec{b} \cdot \nabla B] \\ &+ (\gamma v_{\parallel}) \vec{v}_D \cdot [(\vec{b} \cdot \nabla) \vec{b}] + \gamma \vec{v}_D \cdot [(\vec{v}_D \cdot \nabla) \vec{b}] \\ &+ \gamma \vec{v}_D \cdot \frac{\partial \vec{b}}{\partial t} \end{aligned} \quad (17)$$

$$\gamma = \sqrt{\frac{1}{1 - (v_{\parallel}^2 + v_{\perp}^2 + v_D^2)/c^2}} \quad (18)$$

$$\frac{d\mu}{dt} = 0 \quad (19)$$

where  $\vec{R}$ ,  $\vec{v}_D$ ,  $v_{\parallel}$ ,  $\gamma$ ,  $\vec{b}$  and  $E_{\parallel}$  are the guiding center position, the perpendicular (to the magnetic field) drift velocity, the (parallel) velocity along the magnetic field, the relativistic

gamma factor ( $\gamma = 1/\sqrt{1 - v^2/c^2}$ ), the magnetic field unit vector  $\vec{b} = \vec{B}/B$  and the parallel electric field ( $\vec{E} \cdot \vec{b}$ ), respectively. In Eq. (16),  $\vec{v}_E$  corresponds to the local  $\vec{E} \times \vec{B}$  drift velocity  $\vec{v}_E = (\vec{E} \times \vec{B})/B^2$ . The other terms of Eq. (16) describe the magnetic curvature drift velocity, the gradient drift velocity and so on. The factor  $k = \sqrt{1 - v_E^2/c^2} \simeq 1$  relates the electromagnetic fields to the reference frame moving with  $\vec{v}_E$ . Finally,  $\mu = (\gamma v_\perp)^2/(2B)$  is the relativistic magnetic moment per mass unit with  $v_\perp$  being the particle's gyration velocity in the direction perpendicular to  $\vec{B}$ . The electron kinetic energy can be expressed using the relativistic  $\gamma$ -factor as  $E_k = (\gamma - 1)mc^2$ . We solve Eqs. (15) to (19) utilizing a fourth-order Runge-Kutta scheme. The electromagnetic fields obtained by the MHD simulations are linearly interpolated to the electron positions between the grid points.

Due to the small non-relativistic drift speeds  $\vec{v}_D \approx \vec{v}_E < 2V_0$ , the electron kinetic energy  $E_k$  is proportional to  $v_\parallel^2 + v_\perp^2 + v_D^2 \simeq v_\parallel^2 + v_\perp^2$ . The resulting energy change rates in the parallel and perpendicular directions are given, respectively, by:

$$\begin{aligned} \frac{1}{2} \frac{d(\gamma v_\parallel)^2}{dt} &= \frac{q}{m} \gamma v_\parallel E_\parallel - \mu v_\parallel (\vec{b} \cdot \nabla B) \\ &\quad + (\gamma v_\parallel)^2 \vec{v}_D \cdot [(\vec{b} \cdot \nabla) \vec{b}] + \gamma^2 v_\parallel \vec{v}_D \cdot [(\vec{v}_D \cdot \nabla) \vec{b}] \\ &\quad + \gamma^2 v_\parallel \vec{v}_D \cdot \frac{\partial \vec{b}}{\partial t} \end{aligned} \quad (20)$$

$$\begin{aligned} \frac{1}{2} \frac{d(\gamma v_\perp)^2}{dt} &= \frac{d\mu B}{dt} = \mu \frac{dB}{dt} \\ &= \mu \frac{\partial B}{\partial t} + \mu v_\parallel (\vec{b} \cdot \nabla B) + \mu \vec{v}_D \cdot \nabla B \end{aligned} \quad (21)$$

And the total rate of kinetic energy change is given by:

$$\begin{aligned} \frac{dE_k}{dt} &= \vec{v} \cdot \frac{d\vec{P}}{dt} = \frac{m}{2\gamma} \frac{d(\gamma v)^2}{dt} \\ &\cong \frac{m}{\gamma} \frac{1}{2} \frac{d(\gamma v_\parallel)^2 + (\gamma v_\perp)^2}{dt} \\ &= q v_\parallel E_\parallel + (m \gamma v_\parallel^2) \vec{v}_D \cdot [(\vec{b} \cdot \nabla) \vec{b}] \\ &\quad + (m \gamma v_\parallel) \vec{v}_D \cdot [(\vec{v}_D \cdot \nabla) \vec{b}] + \frac{m \mu}{\gamma} \vec{v}_D \cdot \nabla B \\ &\quad + (m \gamma v_\parallel) \vec{v}_D \cdot \frac{\partial \vec{b}}{\partial t} + \frac{m \mu}{\gamma} \frac{\partial B}{\partial t} \end{aligned} \quad (22)$$

As one can see in Eq. (22), electrons can gain energy by parallel electric fields ( $q v_\parallel E_\parallel$  term), due to magnetic field curvature ( $m \gamma v_\parallel^2 \vec{v}_D \cdot [(\vec{b} \cdot \nabla) \vec{b}]$  term), by curvature drift acceleration ( $m \gamma v_\parallel \vec{v}_D \cdot [(\vec{v}_D \cdot \nabla) \vec{b}]$  term), by (perpendicular) gradient acceleration ( $m \mu (\vec{v}_D \cdot \nabla B)/\gamma$  term),

and temporal variation of the magnetic field, here  $m\gamma v_{\parallel} \vec{v}_D \cdot (\partial \vec{b} / \partial t)$  and  $m\mu(\partial B / \partial t) / \gamma$  terms for the parallel and perpendicular acceleration, respectively. The parallel magnetic field gradient  $(m\mu)[v_{\parallel}(\vec{b} \cdot \nabla B)] / \gamma$  can change the parallel and perpendicular energies simultaneously and transfer energy between them while it does not change the total particle energy.

For our calculations, we inject  $1.7 \times 10^5$  electrons at  $t = 0$  randomly distributed along the midplane of the CS (see the first panel of Fig. 1). The cosines of electrons' initial pitch angle randomly vary in the range of  $[-1, 1]$ . The initial energies are uniformly distributed between 10 eV and 10 keV. Electrons are traced until  $9 t_0$  ( $\sim 9s$ ), the typical duration of electron bursts in the Hermean magnetotail.

## B. Acceleration features

Fig. 2 depicts the temporal evolution of the different contributing acceleration mechanisms of electrons in dependence on the turbulence parameters (see Table I). In the laminar reconnection limit (Case A), resistive electric fields  $E_{\parallel} = \eta J_{\parallel}$  do not significantly accelerate electrons. Instead, mainly the temporal variation of the magnetic field (the  $\mu(\partial B / \partial t) / \gamma$  term) energizes electrons. In case of weak turbulence (small coefficient  $C_{\beta}$ , Case B), the  $E_{\parallel}$  acceleration is slightly enhanced but it is still smaller than the acceleration by  $\partial B / \partial t$ . The overall acceleration in Case B is as efficient as in Case A. The parallel kinetic energy  $E_{k\parallel}$  is reduced in both Cases A and B due to the effect of the parallel gradient  $\mu[v_{\parallel}(\vec{b} \cdot \nabla B)] / \gamma$ , which transfers kinetic energy from the parallel to the perpendicular electron motion.

Stronger turbulence (larger coefficients  $C_{\beta}$  and/or  $\tau$ , Cases C, D and E) acts as enhanced localized anomalous resistivity as well as electron acceleration via the larger EMF  $\vec{\varepsilon}_M$ , where electron acceleration is mainly due to the parallel electric field ( $E_{\parallel}$ ). By comparing Cases C and E, one can find that electron acceleration is enhanced with the enhancement of the turbulence ( $C_{\beta}$ ). The difference between Cases D and E is that the  $\omega$ - and  $\alpha$ -terms (see Eq. (12)) in Case D are two times as large as in Case E, while the  $\beta$ -term contribution remains unchanged. Larger  $\omega$ - and  $\alpha$ -terms indicate weaker magnetic flux annihilation, and therefore the effects of the  $\beta$ -term and EMF  $\vec{\varepsilon}_M$  in Eq. (12) are reduced (Sect. II). Comparing with Case D, hence, electrons in Case E are accelerated to higher energies  $\sim 70$  keV.

In any case, in addition to the acceleration by the parallel electric fields ( $E_{\parallel}$ ), acceleration

effects due to  $\partial B/\partial t$  and  $v_{\parallel}(\vec{b} \cdot \nabla B)$  are important, which lead to electron energization in the direction perpendicular to the magnetic field (see Eq. (21)). Comparing with the  $E_{\parallel}$  acceleration,  $\partial B/\partial t$  and  $v_{\parallel}(\vec{b} \cdot \nabla B)$  accelerations depend, however, very weakly on the turbulence level. Due to the enhanced parallel velocity  $v_{\parallel}$  by  $E_{\parallel}$  acceleration, the energy gain from the  $\partial B/\partial t$  ( $v_{\parallel}(\vec{b} \cdot \nabla B)$ ) term slightly decreases (increases) from Case A to E. The curvature  $\vec{v}_D \cdot [(\vec{b} \cdot \nabla)\vec{b}]$ , perpendicular gradient  $(\vec{v}_D \cdot \nabla B)/\gamma$ , curvature drift  $\vec{v}_D \cdot [(\vec{v}_D \cdot \nabla)\vec{b}]$  and perpendicular gradient  $(\vec{v}_D \cdot \nabla B)/\gamma$  accelerations practically do not contribute to the electron energization.

As a result, for negligible or weak turbulence levels, electrons are mainly accelerated by the temporal variation of the magnetic field ( $\partial B/\partial t$  term) in the chain of plasmoids. In cases of stronger turbulence, however, the parallel electric field ( $E_{\parallel}$ ) acceleration due to the localized EMF  $\vec{\varepsilon}_M$  dominates the electron energization.

### C. Acceleration sites

The bottom five panels of Fig. 3 display the time evolution of the electron total kinetic energy gain ( $\Delta E_k = E_{kt} - E_{k0}$ ) versus the (Z-axis-) position of the electrons for the five different turbulence levels (Cases A to E). The plots localize the electron acceleration sites with respect to the X-points and plasmoid centers (see the stack plot of the vector potential  $A_x$  in the top panel). As one can see the electrons are energized mainly around X-points (black and light blue regions in the top panel), even though the dominant electron acceleration mechanisms are different depending on the turbulence level. That is due to the injection of new reconnecting magnetic flux and strong current density near the X-points to enhance the  $\partial B/\partial t$  and  $E_{\parallel}$  acceleration, respectively. Only a small amount of energy is gained inside the plasmoids, this energization is also mainly due to the temporal variation of the magnetic field  $\partial B/\partial t$ . Acceleration by  $\partial B/\partial t$  in the plasmoids is, however, much weaker than the acceleration processes taking place near the X-points.

The bottom five panels of Fig. 3 illustrate the formations of filamentary structures in the spatial distribution of the energized electrons. The number of the filaments increases with the enhancement of the turbulence. The filaments start at X-points firstly and move then into a channel formed by the split of an X-point (see the top panel). Splitting of X-points indicates the formation of new plasmoids. Therefore, along the filamentary structures, electrons are

first getting accelerated at an X-point and then trapped inside the newly formed and moving secondary plasmoids<sup>29</sup>.

Fig. 4 illustrates this process by showing the trajectory and energy evolution of two characteristic electrons in Case D (similar in Case E). The two electrons are first accelerated by the parallel electric fields ( $E_{\parallel}$ ) at the X-points near  $Z = 100$  and  $-60 L_0$  respectively (see the top and bottom panels). Their accelerations take place mainly at the center of the CS ( $Y = -20 L_0$ ). Since these two electrons are accelerated by  $E_{\parallel}$  at different times  $t$ , the filamentary structures near  $Z = 100$  and  $-60 L_0$  appear at different moments of time (see Fig. 3). Meanwhile the electrons near  $Z = 100 L_0$  spend a longer time in the parallel electric field ( $E_{\parallel}$ ) than those accelerated near  $Z = -60 L_0$ . Therefore, the overall energy gain of the electrons accelerated near  $Z = -60 L_0$  is smaller than that of the electrons accelerated near  $Z = 100 L_0$  despite of the fact that the parallel electric fields ( $E_{\parallel}$ ) are stronger near  $Z = -60 L_0$  (see the slopes of the energy evolution in the third column of Fig. 4).

Although the parallel electric field ( $E_{\parallel}$ ) acceleration dominates the electron energization, it is also interesting to pay attention to their curvature ( $\vec{v}_D \cdot [(\vec{b} \cdot \nabla) \vec{b}]$  term) energization, which leads to the small deceleration of electrons in this study. Animations of their trajectories clearly show that the electrons are affected by the expansion and coalescence of the secondary plasmoids in which they are trapped. At the beginning, the parallel electric field energization enhances the curvature acceleration, leading to its maximum (blue lines in the third column of Fig. 4) near an X-point. Later, however, the electrons are removed from this region along the CS by the newly formed expanded secondary plasmoids. The plasmoid expansion causes a deceleration of the electrons via the curvature term. Almost at the end (after  $8 t_0$ ), plasmoid coalescence again causes electron acceleration which is, however, much smaller than the energy lost due to the plasmoid expansion. Hence, instead of accelerating, the curvature  $\vec{v}_D \cdot [(\vec{b} \cdot \nabla) \vec{b}]$  term decelerates these electrons by four orders of magnitude less than the  $E_{\parallel}$  acceleration.

Previous studies concluded that the curvature  $\vec{v}_D \cdot [(\vec{b} \cdot \nabla) \vec{b}]$  in the plasmoids can significantly contribute to the particle energization at large (MHD) scales<sup>54</sup>. We found, however, that the contribution of the curvature  $\vec{v}_D \cdot [(\vec{b} \cdot \nabla) \vec{b}]$  term is negligibly small. As Fig. 1 demonstrates the plasmoid expansion dominates the reconnection process despite of multiple contractions and coalescences of the plasmoids. That is the reason for the weak contribution of the curvature  $\vec{v}_D \cdot [(\vec{b} \cdot \nabla) \vec{b}]$  acceleration in turbulent plasmoid reconnection (Fig. 2).

## D. Energy spectra

Fig. 5 depicts the number distribution of energetic electrons in the space of the initial ( $E_{k0}$ ) and final ( $E_{kf}$ ) kinetic energy in cases of strong turbulence (Cases C and E). White lines  $E_{k0} = E_{kf}$  divide accelerated (above  $E_{kf} = E_{k0}$ ) and decelerated (below  $E_{kf} = E_{k0}$ ) electrons. Due to the small EMF  $\overrightarrow{\varepsilon_M}$  in Cases A and B, most electrons in these two cases maintain their initial energies and distribute near the line  $E_{kf} = E_{k0}$ . The electron distribution in Cases D and E, on the other hand, are similar, so Case D is not shown in Fig. 5. Kinetic energy  $E_{kf}$  of most electrons in Cases C, D and E stays below 20 keV, a smaller number of electrons can be accelerated up to 60 keV. In these three cases, the most energetic electrons are homogeneously distributed in the  $E_{k0}$  space. This means that the electrons are accelerated to higher energies independent on their initial energies  $E_{k0}$ <sup>54</sup>.

The five panels of Fig. 6 show the evolution of the electron energy spectra for the five different turbulence levels. We calculate the energy spectra by assigning a statistical weight  $\psi(E_k)$  to each electron. The weight function  $\psi(E_k)$  depends on the initial electron energy  $E_{k0}$  as  $\psi(E_k) = \sqrt{E_{k0}} \exp(-E_{k0}/E_{th})$ . We choose  $E_{th} \sim 0.06 keV$  to match with the typical electron thermal energy observed in the Hermean magnetotail. The initial energy distribution is, therefore, Maxwellian (shown as a blue line in each panel of Fig. 6). One can see that the final electron energy spectra strongly depend on the strength of turbulence. In accordance with the results discussed in Sect. III B, the spectra of electrons energized in weakly turbulent CSs (negligible or small EMF  $\overrightarrow{\varepsilon_M}$ , Cases A and B) do not differ much from the initial Maxwellian distribution. In these cases, electrons are only slightly heated due to the (small) background resistivity  $\eta$ . In contrast, for strong turbulence (larger EMF  $\overrightarrow{\varepsilon_M}$ , Cases C, D and E), power-law spectra are formed at energies above 100 eV with a spectral index  $\delta \sim 2.1$  in Case C and 1.7 - 1.8 in Cases D and E. The stronger turbulent EMF  $\overrightarrow{\varepsilon_M}$ , the harder the spectrum of energetic electrons becomes.

## IV. CONCLUSIONS AND DISCUSSIONS

Recently, *Widmer et al.*<sup>31</sup> revealed how turbulence can enhance reconnection rates via the electromotive force (EMF  $\overrightarrow{\varepsilon_M}$ ) with the mean-field turbulence model of *Yoshizawa*<sup>9</sup> and *Yokoi & Hoshino*<sup>10</sup>. We now found that in strong turbulence, the turbulence driven EMF

$\vec{\varepsilon}_M$  can also cause efficient electron acceleration via the enhanced localized parallel electric fields ( $E_{\parallel}$ ) near X-points here (Cases C, D and E). Power-law spectra up to 60 keV form out of an initial Maxwellian distribution with a thermal electron energy 60 eV typical for the Hermean magnetotail. If other typical parameters of the Hermean magnetotail are considered, the spectral indices of the power-law spectra are between 1.68 - 2.14. The higher the turbulence level, the harder the electron spectrum. Indeed, energetic electron distributions in the Hermean magnetotail observed by MESSENGER often show power-law indices between 1.5 and 4<sup>15-17</sup>. Turbulence contributes to the electron energization via the EMF  $\vec{\varepsilon}_M$ , in a similar way as a localized anomalous resistivity<sup>55,56</sup>. On the other hand, for weak turbulence (negligible or small EMF  $\vec{\varepsilon}_M$ , here Cases A and B), the rate of the change of the magnetic-field ( $\partial B/\partial t$ ) dominates the electron energization, but the electrons just become heated and not significantly accelerated.

Previous studies<sup>54,57,58</sup> have found that electron acceleration is dominated by parallel electric field ( $E_{\parallel}$ ) assuming large "anomalous" resistivities. We found that strong acceleration is mainly due to a localized turbulent EMF  $\vec{\varepsilon}_M$ . Parallel electric fields ( $E_{\parallel}$ ) in strong turbulence and magnetic field variations ( $\partial B/\partial t$ ) both accelerate electrons mainly near the reconnection X-lines, where current density and compression of the magnetic flux reach their maxima.  $\partial B/\partial t$  term can accelerate electrons also inside plasmoids, but its overall efficiency is much weaker than the acceleration near X-points. Curvature  $\vec{v}_D \cdot [(\vec{b} \cdot \nabla) \vec{b}]$  acceleration due to the contraction and coalescence of plasmoids, however, does not contribute significantly to the electron acceleration in case of turbulent plasmoid reconnection, since the plasmoid expansion dominates the plasmoid reconnection process, slowing down the electrons.

Our results provide evidence that turbulence not only enhances the rate of magnetic reconnection but also efficiently accelerates electrons if the turbulence is strong enough. This complements, e.g., the study of *Kowal et al.*<sup>8</sup>, who used a different turbulence model applied to the acceleration processes in the interstellar medium (ISM). Our findings also complement previous studies<sup>19,59,60</sup> of particle acceleration in the Hermean magnetotail, which did not consider turbulence, while turbulence is ubiquitous in collisionless plasmas.

Note that the parametrizations of the turbulence by the coefficients  $C_{\beta}$  and  $\tau$  is based on previous studies. In order to address the effects of the turbulence on electron acceleration in plasmoid-unstable CSs and test the electron acceleration results in this paper, more detailed self-consistent studies with the mean-field turbulence model will have to be carried out

in the future. Meanwhile the parametrizations of the turbulence for which we found the most efficient electron acceleration may serve as a reference for future detailed studies of the turbulent plasmoid reconnection. At least they provide upper limits for electron acceleration by the turbulent plasmoid reconnection which can be expected to be measured by the Bepi Colombo mission to Mercury to be launched soon.

## ACKNOWLEDGMENTS

X. Zhou thanks the Max-Planck-Society for granting her a postdoc-stipend. F. Widmer acknowledges the IMPRS School at the Max Planck Institute for Solar System Research for the financial support at the time of this work. J. Büchner and P. A. Muñoz acknowledge financial support from the Max-Planck-Princeton Center for Plasma Physics and the DFG Schwerpunktprogramm "PlanetMag" SPP 1488.

## REFERENCES

- <sup>1</sup>W. H. Matthaeus and S. L. Lamkin, "Rapid magnetic reconnection caused by finite amplitude fluctuations," *Phys. Fluids* **28**, 303–307 (1985).
- <sup>2</sup>A. Lazarian and E. T. Vishniac, "Reconnection in a Weakly Stochastic Field," *Astrophys. J.* **517**, 700–718 (1999), astro-ph/9811037.
- <sup>3</sup>J. Ambrosiano, W. H. Matthaeus, M. L. Goldstein, and D. Plante, "Test particle acceleration in turbulent reconnecting magnetic fields," *J. Geophys. Res.* **93**, 14383 (1988).
- <sup>4</sup>P. Dmitruk, W. H. Matthaeus, and N. Seenu, "Test Particle Energization by Current Sheets and Nonuniform Fields in Magnetohydrodynamic Turbulence," *Astrophys. J.* **617**, 667–679 (2004).
- <sup>5</sup>P. Petkaki and A. L. MacKinnon, "Particle acceleration by fluctuating electric fields at a magnetic field null point," *Astron. Astrophys.* **472**, 623–632 (2007).
- <sup>6</sup>P. Petkaki and A. L. MacKinnon, "Acceleration of charged particles by fluctuating and steady electric fields in a X-type magnetic field," *Adv. Space Res.* **48**, 884–898 (2011).
- <sup>7</sup>C. A. Burge, P. Petkaki, and A. L. MacKinnon, "Particle Acceleration in the Presence of Weak Turbulence at an X-Type Neutral Point," *Sol. Phys.* **280**, 575–590 (2012).
- <sup>8</sup>G. Kowal, E. M. de Gouveia Dal Pino, and A. Lazarian, "Particle Acceleration in Tur-



- bulence and Weakly Stochastic Reconnection,” *Phys. Rev. Lett.* **108**, 241102 (2012), arXiv:1202.5256 [astro-ph.HE].
- <sup>9</sup>A. Yoshizawa, “Self-consistent turbulent dynamo modeling of reversed field pinches and planetary magnetic fields,” *Phys. Fluids B* **2**, 1589–1600 (1990).
- <sup>10</sup>N. Yokoi and M. Hoshino, “Flow-turbulence interaction in magnetic reconnection,” *Phys. Plasmas* **18**, 111208–111208 (2011), arXiv:1105.6343 [astro-ph.SR].
- <sup>11</sup>J. Birn, A. V. Artemyev, D. N. Baker, M. Echim, M. Hoshino, and L. M. Zelenyi, “Particle Acceleration in the Magnetotail and Aurora,” *Space Sci. Rev.* **173**, 49–102 (2012).
- <sup>12</sup>J. H. Eraker and J. A. Simpson, “Acceleration of charged particles in Mercury’s magnetosphere,” *J. Geophys. Res.* **91**, 9973–9993 (1986).
- <sup>13</sup>T. P. Armstrong, S. M. Krimigis, and L. J. Lanzerotti, “A reinterpretation of the reported energetic particle fluxes in the vicinity of Mercury,” *J. Geophys. Res.* **80**, 4015–4017 (1975).
- <sup>14</sup>E. Kirsch and A. K. Richter, “Possible detection of low energy ions and electrons from planet Mercury by the HELIOS spacecraft,” *Annales Geophysicae* **3**, 13–18 (1985).
- <sup>15</sup>G. C. Ho, S. M. Krimigis, R. E. Gold, D. N. Baker, J. A. Slavin, B. J. Anderson, H. Korth, R. D. Starr, D. J. Lawrence, R. L. McNutt, and S. C. Solomon, “MESSENGER Observations of Transient Bursts of Energetic Electrons in Mercury’s Magnetosphere,” *Science* **333**, 1865–1868 (2011).
- <sup>16</sup>G. C. Ho, S. M. Krimigis, R. E. Gold, D. N. Baker, B. J. Anderson, H. Korth, J. A. Slavin, R. L. McNutt, Jr., R. M. Winslow, and S. C. Solomon, “Spatial distribution and spectral characteristics of energetic electrons in Mercury’s magnetosphere,” *J. Geophys. Res. Space Phys.* **117**, A00M04 (2012).
- <sup>17</sup>D. J. Lawrence, B. J. Anderson, D. N. Baker, W. C. Feldman, G. C. Ho, H. Korth, R. L. McNutt, P. N. Peplowski, S. C. Solomon, R. D. Starr, J. D. Vandegriff, and R. M. Winslow, “Comprehensive survey of energetic electron events in Mercury’s magnetosphere with data from the MESSENGER Gamma-Ray and Neutron Spectrometer,” *J. Geophys. Res. Space Phys.* **120**, 2851–2876 (2015).
- <sup>18</sup>D. N. Baker, R. M. Dewey, D. J. Lawrence, J. O. Goldsten, P. N. Peplowski, H. Korth, J. A. Slavin, S. M. Krimigis, B. J. Anderson, G. C. Ho, R. L. McNutt, J. M. Raines, D. Schriver, and S. C. Solomon, “Intense energetic electron flux enhancements in Mercury’s magnetosphere: An integrated view with high-resolution observations from MESSENGER,” *J. Geophys. Res. Space Phys.* **121**, 2171–2184 (2016).

- <sup>19</sup>D. C. Delcourt, K. Seki, N. Terada, and Y. Miyoshi, “Electron dynamics during substorm dipolarization in Mercury’s magnetosphere,” *Ann. Geophys.* **23**, 3389–3398 (2005).
- <sup>20</sup>L. M. Zelenyi, J. G. Lominadze, and A. L. Taktakishvili, “Generation of the energetic proton and electron bursts in planetary magnetotails,” *J. Geophys. Res.* **95**, 3883–3891 (1990).
- <sup>21</sup>L. Zelenyi, M. Oka, H. Malova, M. Fujimoto, D. Delcourt, and W. Baumjohann, “Particle Acceleration in Mercury’s Magnetosphere,” *Space Sci. Rev.* **132**, 593–609 (2007).
- <sup>22</sup>J. A. Slavin, M. H. Acuna, B. J. Anderson, D. N. Baker, M. Benna, S. A. Boardsen, G. Gloeckler, R. E. Gold, G. C. Ho, H. Korth, S. M. Krimigis, R. L. McNutt, J. M. Raines, M. Sarantos, D. Schriver, S. C. Solomon, P. Travnicek, and T. H. Zurbuchen, “MESSENGER Observations of Magnetic Reconnection in Mercury’s Magnetosphere,” *Science* **324**, 606–610 (2009).
- <sup>23</sup>G. A. DiBraccio, J. A. Slavin, S. M. Imber, D. J. Gershman, J. M. Raines, C. M. Jackman, S. A. Boardsen, B. J. Anderson, H. Korth, T. H. Zurbuchen, R. L. McNutt, and S. C. Solomon, “MESSENGER observations of flux ropes in Mercury’s magnetotail,” *Planetary Space Science* **115**, 77–89 (2015).
- <sup>24</sup>W. J. Sun, S. Y. Fu, J. A. Slavin, J. M. Raines, Q. G. Zong, G. K. Poh, and T. H. Zurbuchen, “Spatial distribution of Mercury’s flux ropes and reconnection fronts: MESSENGER observations,” *J. Geophys. Res. Space Phys.* **121**, 7590–7607 (2016).
- <sup>25</sup>N. F. Loureiro, A. A. Schekochihin, and S. C. Cowley, “Instability of current sheets and formation of plasmoid chains,” *Phys. Plasmas* **14**, 100703 (2007), astro-ph/0703631.
- <sup>26</sup>D. A. Uzdensky, N. F. Loureiro, and A. A. Schekochihin, “Fast Magnetic Reconnection in the Plasmoid-Dominated Regime,” *Phys. Rev. Lett.* **105**, 235002 (2010), arXiv:1008.3330 [astro-ph.SR].
- <sup>27</sup>M. Hoshino, A. Nishida, T. Yamamoto, and S. Kokubun, “Turbulent magnetic field in the distant magnetotail: Bottom-up process of plasmoid formation?” *Geophys. Res. Lett.* **21**, 2935–2938 (1994).
- <sup>28</sup>M. Karlický, “Series of high-frequency slowly drifting structures mapping the flare magnetic field reconnection,” *Astron. Astrophys.* **417**, 325–332 (2004).
- <sup>29</sup>M. Bárta, J. Büchner, M. Karlický, and J. Skála, “Spontaneous Current-layer Fragmentation and Cascading Reconnection in Solar Flares. I. Model and Analysis,” *Astrophys. J.* **737**, 24 (2011), arXiv:1011.4035 [astro-ph.SR].

- <sup>30</sup>M. Karlický, M. Bárta, and D. Nickeler, “Fragmentation during merging of plasmoids in the magnetic field reconnection,” *Astron. Astrophys.* **541**, A86 (2012).
- <sup>31</sup>F. Widmer, J. Büchner, and N. Yokoi, “Characterizing plasmoid reconnection by turbulence dynamics,” *Phys. Plasmas* **23**, 092304 (2016).
- <sup>32</sup>J. F. Drake, M. Swisdak, H. Che, and M. A. Shay, “Electron acceleration from contracting magnetic islands during reconnection,” *Nature (London)* **443**, 553–556 (2006).
- <sup>33</sup>J. F. Drake, M. Swisdak, and R. Fermo, “The Power-law Spectra of Energetic Particles during Multi-island Magnetic Reconnection,” *Astrophys. J.* **763**, L5 (2013), arXiv:1210.4830 [astro-ph.SR].
- <sup>34</sup>M. Oka, T.-D. Phan, S. Krucker, M. Fujimoto, and I. Shinohara, “Electron Acceleration by Multi-Island Coalescence,” *Astrophys. J.* **714**, 915–926 (2010), arXiv:1004.1154 [astro-ph.SR].
- <sup>35</sup>K. G. Tanaka, M. Fujimoto, S. V. Badman, and I. Shinohara, “Dynamic magnetic island coalescence and associated electron acceleration,” *Physics of Plasmas* **18**, 022903 (2011).
- <sup>36</sup>X. Zhou, J. Büchner, M. Bárta, W. Gan, and S. Liu, “Electron Acceleration by Cascading Reconnection in the Solar Corona. I. Magnetic Gradient and Curvature Drift Effects,” *Astrophys. J.* **815**, 6 (2015), arXiv:1504.06486 [astro-ph.SR].
- <sup>37</sup>S. E. Guidoni, C. R. DeVore, J. T. Karpen, and B. J. Lynch, “Magnetic-island Contraction and Particle Acceleration in Simulated Eruptive Solar Flares,” *Astrophys. J.* **820**, 60 (2016), arXiv:1603.01309 [astro-ph.SR].
- <sup>38</sup>D. Borovikov, V. Tenishev, T. I. Gombosi, S. E. Guidoni, C. R. DeVore, J. T. Karpen, and S. K. Antiochos, “Electron Acceleration in Contracting Magnetic Islands during Solar Flares,” *Astrophys. J.* **835**, 48 (2017).
- <sup>39</sup>W. Schmidt, “Large Eddy Simulations in Astrophysics,” *Living Rev. Comput. Astrophys.* **1**, 2 (2015), arXiv:1404.2483.
- <sup>40</sup>J. Skála, F. Baruffa, J. Büchner, and M. Rampp, “The 3D MHD code GOEMHD3 for astrophysical plasmas with large Reynolds numbers. Code description, verification, and computational performance,” *Astron. Astrophys.* **580**, A48 (2015).
- <sup>41</sup>F. Widmer, J. Büchner, and N. Yokoi, “Sub-grid-scale description of turbulent magnetic reconnection in magnetohydrodynamics,” *Phys. Plasmas* **23**, 042311 (2016), arXiv:1511.04347 [physics.plasm-ph].
- <sup>42</sup>M. Fujimoto, W. Baumjohann, K. Kabin, R. Nakamura, J. A. Slavin, N. Terada, and

- L. Zelenyi, “Hermean Magnetosphere-Solar Wind Interaction,” *Space Sci. Rev.* **132**, 529–550 (2007).
- <sup>43</sup>F. Krause and K.-H Rädler, *Mean-Field Magnetohydrodynamics and Dynamo Theory* (Pergamon Press Ltd, Berlin, 1980).
- <sup>44</sup>N. Yokoi, D. Schmitt, V. Pipin, and F. Hamba, “A New Simple Dynamo Model for Stellar Activity Cycle,” *Astrophys. J.* **824**, 67 (2016), arXiv:1601.06348 [astro-ph.SR].
- <sup>45</sup>N. Yokoi, “Cross helicity and related dynamo,” *Geophysical and Astrophysical Fluid Dynamics* **107**, 114–184 (2013), arXiv:1306.6348 [astro-ph.SR].
- <sup>46</sup>F. Hamba, “One-dimensional calculation of a turbulent dynamo model for reversed field pinches,” *Physics of Fluids B* **2**, 3064–3073 (1990).
- <sup>47</sup>F. Hamba, “Turbulent dynamo effect and cross helicity in magnetohydrodynamic flows,” *Phys. Fluids* **4**, 441–450 (1992).
- <sup>48</sup>K. Higashimori, N. Yokoi, and M. Hoshino, “Explosive Turbulent Magnetic Reconnection,” *Phys. Rev. Lett.* **110**, 255001 (2013), arXiv:1305.6695 [astro-ph.EP].
- <sup>49</sup>F. Krause and K.-H. Raedler, *Mean-field magnetohydrodynamics and dynamo theory* (Pergamon Press Ltd, Berlin, 1980).
- <sup>50</sup>P. G. Watson, S. Oughton, and I. J. D. Craig, “The impact of small-scale turbulence on laminar magnetic reconnection,” *Physics of Plasmas* **14**, 032301 (2007).
- <sup>51</sup>J. Büchner and L. M. Zelenyi, “Regular and chaotic charged particle motion in magnetotail-like field reversals. I - Basic theory of trapped motion,” *J. Geophys. Res.* **94**, 11821–11842 (1989).
- <sup>52</sup>J. Büchner and L. M. Zelenyi, “Regular and chaotic particle motion in sheared magnetic field reversals,” *Adv. Sp. Res.* **11**, 177–182 (1991).
- <sup>53</sup>T. G. Northrop, *Interscience Publishers, 1963, 109 p.* (Interscience Publishers, 1963).
- <sup>54</sup>X. Zhou, J. Büchner, M. Bárta, W. Gan, and S. Liu, “Electron Acceleration by Cascading Reconnection in the Solar Corona. II. Resistive Electric Field Effects,” *Astrophys. J.* **827**, 94 (2016).
- <sup>55</sup>M. Gordovskyy, P. K. Browning, and G. E. Vekstein, “Particle acceleration in a transient magnetic reconnection event,” *Astron. Astrophys.* **519**, A21 (2010).
- <sup>56</sup>L.-P. Yang, L.-H. Wang, J.-S. He, C.-Y. Tu, S.-H. Zhang, L. Zhang, and X.-S. Feng, “Numerical simulation of superhalo electrons generated by magnetic reconnection in the solar wind source region,” *Research in Astronomy and Astrophysics* **15**, 348 (2015),

arXiv:1406.4233 [astro-ph.SR].

- <sup>57</sup>R. Turkmani, P. J. Cargill, K. Galsgaard, L. Vlahos, and H. Isliker, “Particle acceleration in stochastic current sheets in stressed coronal active regions,” *Astron. Astrophys.* **449**, 749–757 (2006).
- <sup>58</sup>M. Gordovsky, P. K. Browning, and G. E. Vekstein, “Particle Acceleration in Fragmenting Periodic Reconnecting Current Sheets in Solar Flares,” *Astrophys. J.* **720**, 1603–1611 (2010).
- <sup>59</sup>D. Schriver, P. M. Trávníček, B. J. Anderson, M. Ashour-Abdalla, D. N. Baker, M. Benna, S. A. Boardsen, R. E. Gold, P. Hellinger, G. C. Ho, H. Korth, S. M. Krimigis, R. L. McNutt, J. M. Raines, R. L. Richard, J. A. Slavin, S. C. Solomon, R. D. Starr, and T. H. Zurbuchen, “Quasi-trapped ion and electron populations at Mercury,” *Geophys. Res. Lett.* **38**, L23103 (2011).
- <sup>60</sup>B. M. Walsh, A. S. Ryou, D. G. Sibeck, and I. I. Alexeev, “Energetic particle dynamics in Mercury’s magnetosphere,” *J. Geophys. Res. Space Phys.* **118**, 1992–1999 (2013).

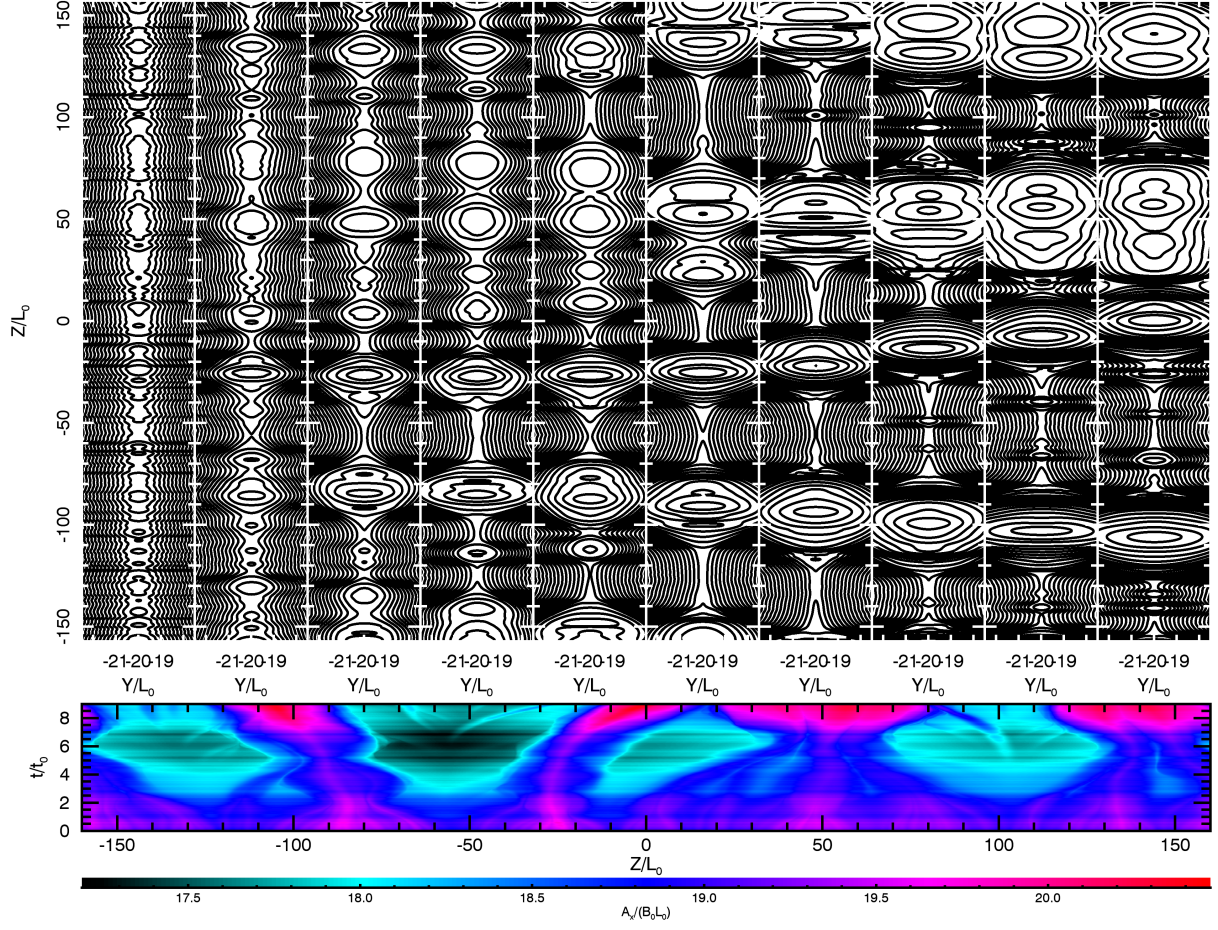


FIG. 1. Top: evolution of the mean magnetic field around the midplane ( $y = -20L_0$ ) of the plasmoid-unstable CS. Bottom shows the stack plot of the out-of-plane vector potential component  $A_x$  along the midplane of the CS  $y = -20 L_0$ , which is also a proxy of the evolution of the reconnection electric field  $E_x$ .

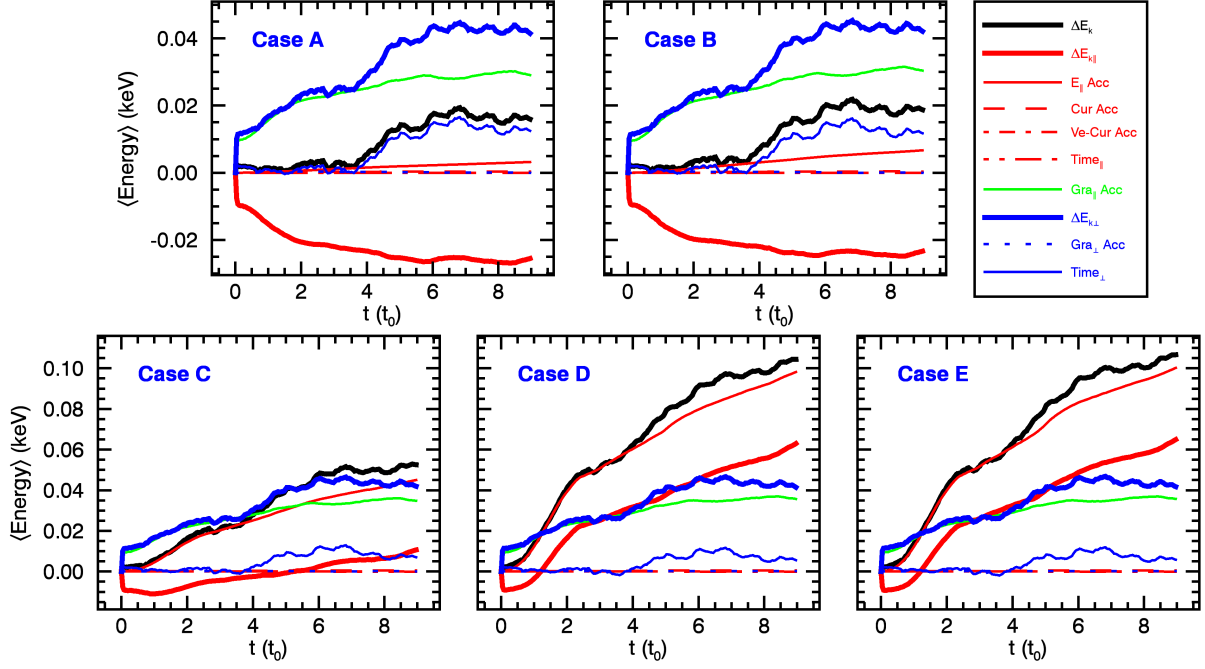


FIG. 2. Average contribution of the different acceleration terms to the electron energy gain: Total energy  $\Delta E_k = E_{kt} - E_{k0}$  (thick black lines), gain in the parallel direction  $\Delta E_{k||} = E_{k||t} - E_{k||0}$  (thick red lines), perpendicular energy gain  $\Delta E_{k\perp} = E_{k\perp t} - E_{k\perp 0}$  (thick blue lines). The acceleration terms are: parallel electric field acceleration (thin red lines), magnetic curvature acceleration (red dashed lines), curvature drift acceleration (red dash-dot lines), time change effects in the parallel direction (red dash-dot-dot-dot lines), parallel gradient acceleration (cyan lines), perpendicular gradient acceleration (blue dotted lines) as well as magnetic field variation acting in the perpendicular direction (thin blue lines). Note the different range in the y-axis between the panels of the first and second rows.

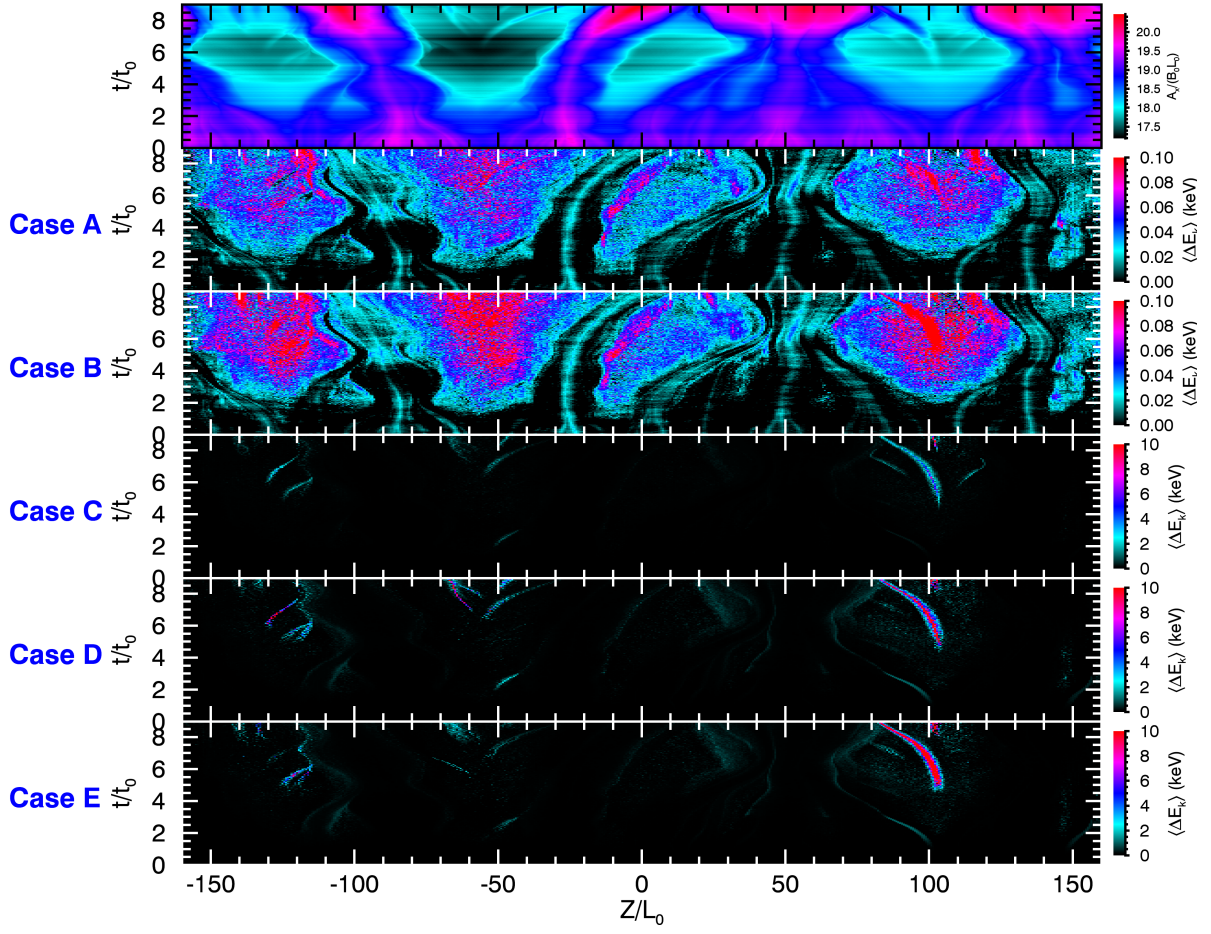


FIG. 3. Top:  $A_x$  stack plot as at the bottom of Fig. 1, indicating the location of X- and O-lines inside plasmoids. Bottom five panels: electron total kinetic energy gain ( $\Delta E_k = E_{kt} - E_{k0}$ ) versus the Z-axis projection of the electron positions at the time  $t$ , in order to visualize their acceleration sites with respect to the X-points and plasmoids. Note the different range in the color scheme between Cases A, B compared with C, D and E.



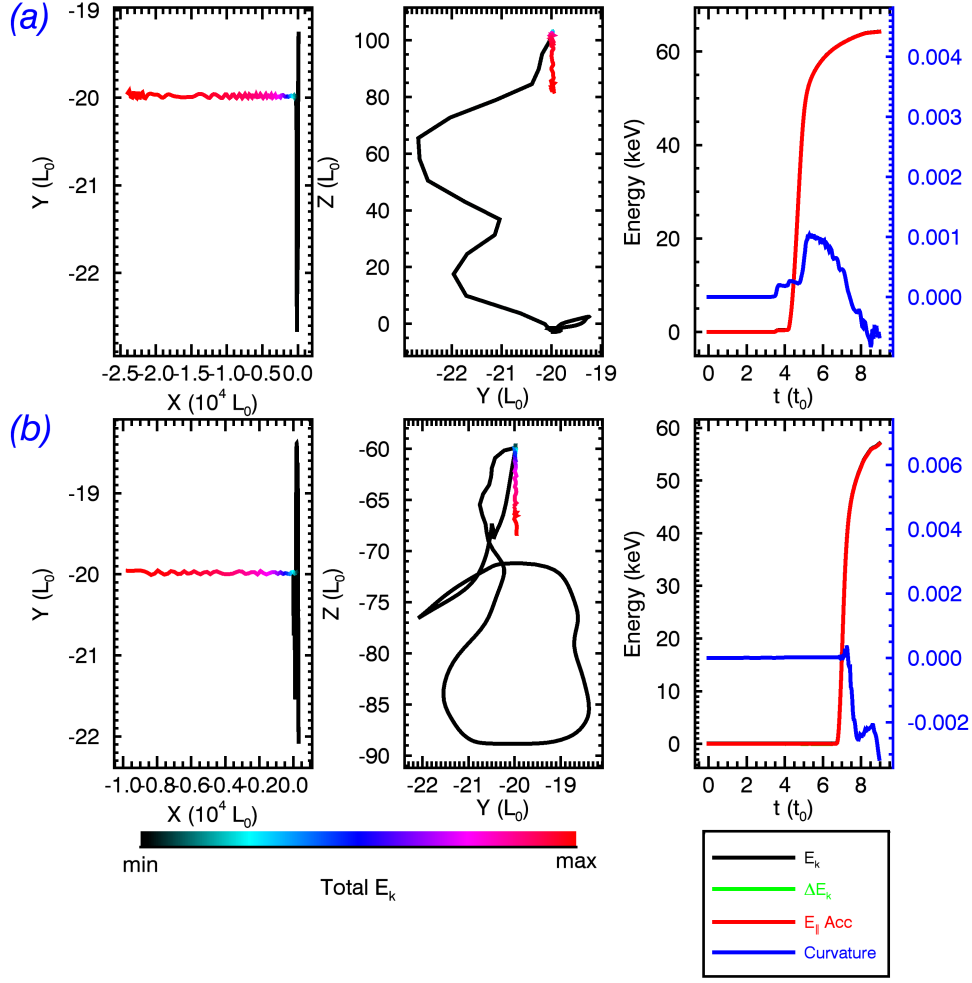


FIG. 4. Trajectory and energy evolution of two characteristic electrons "(a) and (b)" in strong turbulence (Case D). First and second column: projection of the electron trajectories in the  $xy$  and  $yz$  planes. These trajectories are color-coded by their total kinetic energy  $E_k$  profiles. Third column: evolution of  $E_k$  (black line), total energy gain  $\Delta E_k$  (cyan line), parallel electric field acceleration ( $E_{\parallel}$  Acc, red line) and acceleration due to the curvature acceleration (Curvature, blue line). The y-axis in the right side corresponds only to the curvature acceleration. In the animations, the first column shows the location evolution of the electron (red cross) in the CS, the second column is similar to the panels in the third column of Fig.4. Vertical black dashed line in the second column of the animations corresponds to the time of the first column.

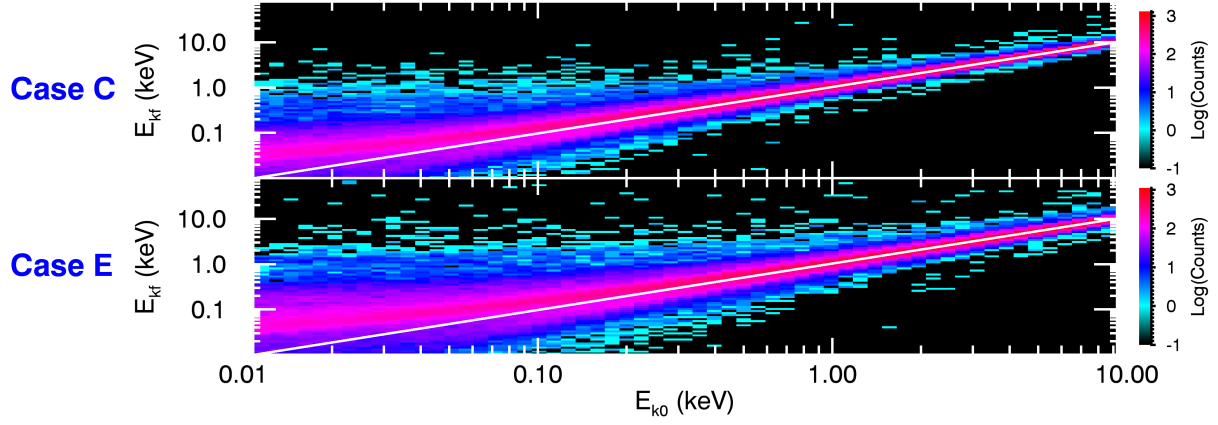


FIG. 5. Number distribution of energetic electrons in the initial-final kinetic energy ( $E_{k0} - E_{kf}$ ) space for the strong turbulence Case C and E. White lines correspond to " $E_{kf} = E_{k0}$ ", separating regions of electron net acceleration and deceleration.

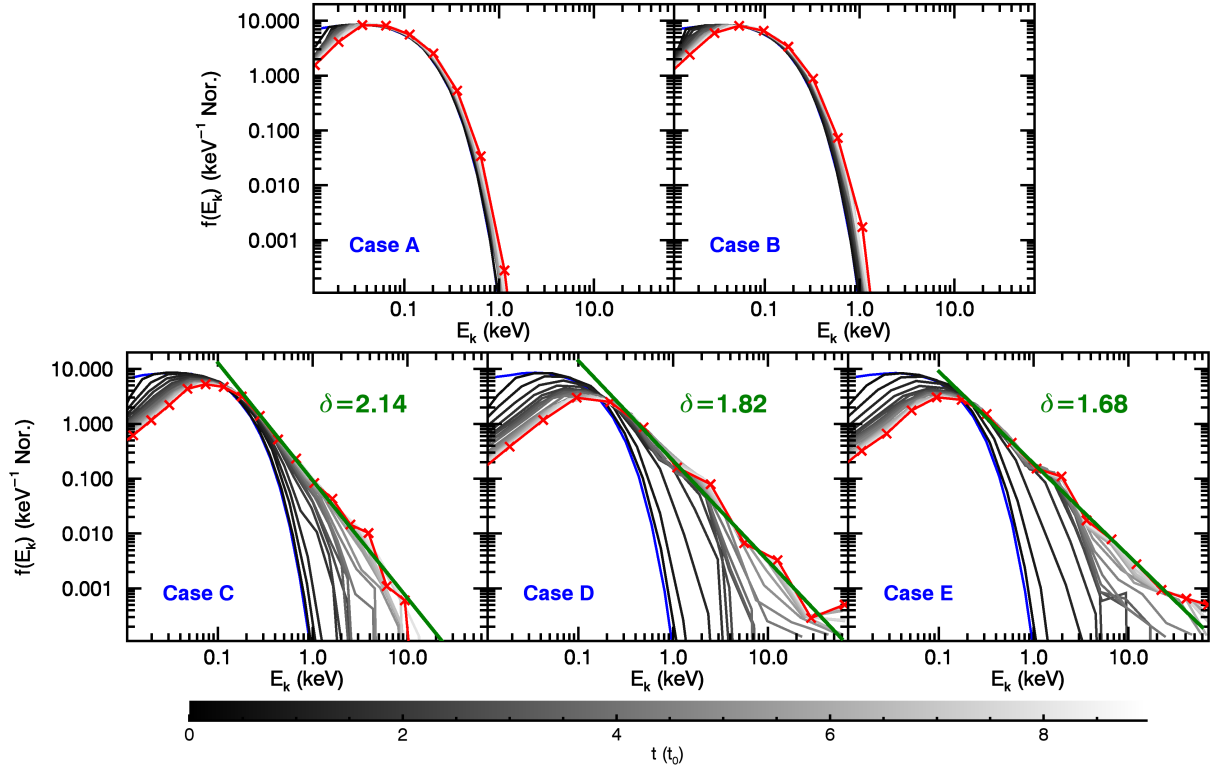


FIG. 6. Electron spectra dependence on the strength of the turbulence. Grayscale is used to distinguish spectra at different time  $t$  (from black to bright). Initial and final electron spectra are highlighted by blue and red lines, respectively. Green lines in the bottom panels are power law fittings with spectral index  $\delta$  given in the corresponding panel.